RESEARCH ARTICLE | MAY 17 2023

Comparison of the effect of suction-injection-combination on Rayleigh–Bénard convection in the case of asymmetric boundaries with those of symmetric ones

C. Kanchana; P. G. Siddheshwar; L. M. Pérez; ... et. al

Physics of Fluids 35, 053615 (2023)
https://doi.org/10.1063/5.0146657

Physics of Fluids ARTICLE pubs.aip.org/aip/pof

Comparison of the effect of suction-injection-combination on Rayleigh–Bénard convection in the case of asymmetric boundaries with those of symmetric ones

Cite as: Phys. Fluids **35**, 053615 (2023); doi: 10.1063/5.0146657
Submitted: 15 February 2023 · Accepted: 29 April 2023 ·
Published Online: 17 May 2023

C. Kanchana,[1,a)] P. G. Siddheshwar,[2] L. M. Pérez,[3] and D. Laroze[1]

AFFILIATIONS

[1]Instituto de Alta Investigación, CEDENNA, Universidad de Tarapacá, Casilla 7 D, Arica, Chile
[2]Center for Mathematical Needs, Department of Mathematics, CHRIST(Deemed to be University), Bengaluru 560029, India
[3]Departamento de Física, FACI, Universidad de Tarapacá, Casilla 7 D, Arica 1000000, Chile

[a)]Author to whom correspondence should be addressed: ckanchana@academicos.uta.cl

ABSTRACT

The effect of suction-injection-combination (SIC) on the linear and weakly nonlinear stability of Rayleigh–Bénard convection is considered in the paper for the cases of symmetric and asymmetric boundary conditions. Using the Maclaurin series with an appropriate number of terms, expression for eigenfunctions is obtained. The linear theory corroborates the results obtained using the chosen eigenfunctions in the limiting case of the no-SIC effect by matching accurately with the exact values concerning the critical Rayleigh number (Ra_c) and the wave number (α_c). It is found that the effect of SIC is to stabilize the system in the case of symmetric boundaries irrespective of SIC being pro-gravity or anti-gravity. However, the effect of SIC is to stabilize/destabilize the system depending on SIC being pro-gravity or anti-gravity in the case of the asymmetric boundaries. We also noted a similar effect in the case of α_c wherein a maximum error of order 10^{-4} was observed. The main novelty of the present work is studying the influence of SIC on the nonlinear dynamics of the considered problem. It is shown that the effect of SIC is to hasten the onset of chaos. Using various indicators (the largest Lyapunov exponent, the time series solution, the amplitude spectrum, and the phase-space plots), the dynamical behavior of the system is analyzed and the influence of SIC on the dynamics is recorded. The change due to the boundary effect and the SIC on the size of convection rolls and the trapping region where the dynamical system evolves within a bound is highlighted in the paper.

I. INTRODUCTION

Any model that is conceptionally rich and accessible to experiment always remains one of the most actively and extensively studied physical systems. One such model is the Rayleigh–Bénard convection system (RBCS), whose dynamics acts as a prototype for many physical situations. In RBCS, convection occurs in a Newtonian fluid (a viscous fluid layer) between two parallel plates due to the temperature difference between the plates (the lower plate is hotter than the upper plate). When the lower plate is heated, the opposing forces of (viscosity, thermal conductivity) and buoyancy (buoyancy, temperature difference) give rise to convective instabilities. This convective instability creates a spatiotemporal non-uniform thermal distribution that leads to the formation of convective cell patterns.[1,2] The non-dimensional parameter, Rayleigh number (Ra), characterizes the onset of a convective cell pattern. The value of Ra at which the convective cell pattern forms is called the critical Rayleigh number (Ra_c), and this value greatly depends on the type of boundary condition prevalent at the plates. For example, in the case of stress free, thermally conducting upper and lower boundaries, $Ra_c = 657.51$ and in the case of rigid, thermally conducting upper and lower boundaries, $Ra_c = 1707$. More information on the boundary conditions' dependence of Ra_c is available in the books by Chandrasekhar[3] and Platten and Legros.[4] Other way of modifying the value of Ra_c is by imposing an internal or external mechanism. One such mechanism is a vertical through-flow or transverse flow achieved by injecting and sucking fluid at the boundaries, which is either pro-gravity or anti-gravity.

The effect of adverse vertical temperature gradient along with imposed vertical mass flux downward through the layer can be observed in earth's atmosphere and below the cloud base.[5,6] The applicability of this type of mathematical model in the earth's atmosphere is demonstrated by Krishnamurti[7] using a laboratory experimental test for Boussinesq fluid between two conducting porous boundaries in the presence of a uniform vertical velocity. She showed that the solution of the linear stability problem for small values of the non-dimensional parameter, named as the Peclet number (Pe), which characterizes the rate of injection and suction of the fluid is infinitely degenerate. The critical Rayleigh number is increased by a term proportional to Pe^2 for large Prandtl number, but it decreases for small Prandtl number. The size of the cell is squashed upward or downward depending upon the sign of Pe being positive or negative.

Gershuni *et al.*[8] considered a homogeneous inward flow (injection) of fluid at the lower rigid, conducting bounding surface and outward flow (suction) of fluid at the upper rigid, conducting bounding surface in the RBCS and studied the influence of the permeable boundaries on the stability of the system using streamline plots. Later, Shvartsblat[9] showed that the Ra expression is a function of Pe. Furthermore, Shvartsblat[9] reported that Ra_c increases as Pe increases and, therefore, argued that the influence of these permeable boundaries is to delay the convective instability. Nield[10] reported that the argument of Shvartsblat[9] is deceptive because the influence of the permeable boundaries greatly depends on the bounding surface being symmetric or asymmetric. Using an appropriate Fourier–Galerkin expansion, Nield[10] reported the asymptotic relation between Ra and Pe for 12 different boundary conditions; FCRC/RCFC, RIFI/FIRI, RCRI/RIRC, RCFI/FIRC, RIFC/FCRI, FCFI/FIFC, where F, R, C, and I denote the free, rigid, conducting, and insulating boundaries. Nield[10] showed that the stabilizing effect of throughflow ceases when the upper and lower boundaries are of different type and the Prandtl number, Pr, is less than or greater than 5/4. Therefore, the dependency of Pr and the bounding surface on throughflow is explained in his seminal work.

Siddheshwar and Pranesh[11] studied the influence of pro-gravity and anti-gravity suction-injection combination (SIC) on the onset of Rayleigh–Bénard–Marangoni convection in fluids with suspended particles and showed that there is a threshold value of Pe, say Pe_c, such that when $Pe < Pe_c$, $M_c^{\text{anti-gravity SIC}} < M_c^{\text{no SIC}}$ and in other cases $M_c^{SIC} > M_c^{\text{no SIC}}$, where M_c is the critical Marangoni number. A similar result on the critical wave number is demonstrated in the paper. Influence of the throughflow on the onset of RBCS for a combustible gaseous mixture is studied by Bayliss *et al.*[12] The corresponding problem for convection in a porous medium has been analyzed by Wooding,[13] Sutton,[14] Homsy and Sherwood,[15] Jones and Persichetti,[16] Shivakumara,[17] Barletta and Nield,[18] and Capone *et al.*[19]

In the present paper, we consider the effect of the SIC on linear and weakly nonlinear stability analyses of RBCS for the cases of symmetric and asymmetric boundary conditions. Laboratory simulations or experiments of RBCS with weak SIC would normally be with either RIRI (symmetric) or RIFI (asymmetric) boundary combination, which are termed as realistic ones. Since it was possible to accurately make such analyses, in the paper it was decided to bring in boundary influences into the investigation.

Using the Maclaurin series with an appropriate number of terms (decided using the ratio test), we arrive at the polynomial eigenfunctions, which describe the convective cells, the horizontal temperature difference in the convective cells, and the distortion of the basic temperature by convection. Influence of the weak SIC on the stability of the system is also studied. The dynamical behavior of the system is analyzed using the indicators: the largest Lyapunov exponent (LLE), the time series, the amplitude spectrum, and the phase-space plots. The drastic change in the influence of the SIC due to the type of boundary conditions is explained. Furthermore, the influence of the SIC and boundary conditions on the boundedness of the solution is highlighted.

II. THE MATHEMATICAL MODEL FOR STUDYING THE RBCS IN THE PRESENCE OF SIC

The RBCS with the SIC in a viscous fluid layer is considered between two infinite extent parallel plates at a distant h apart and having a constant temperatures $T_0 + \Delta T(\Delta T > 0)$ and T_0, respectively, at the lower and the upper plates. The Cartesian coordinate system is assumed with the origin being situated to the lower boundary, and z-axis is directed vertically upward. Two types of homogeneous SIC flow (pro-gravity and anti-gravity) in the vertical direction are considered as shown in Fig. 1. For mathematical tractability, we confine ourselves to two-dimensional rolls so that all physical quantities are independent of y, a horizontal co-ordinate. Furthermore, the boundaries are

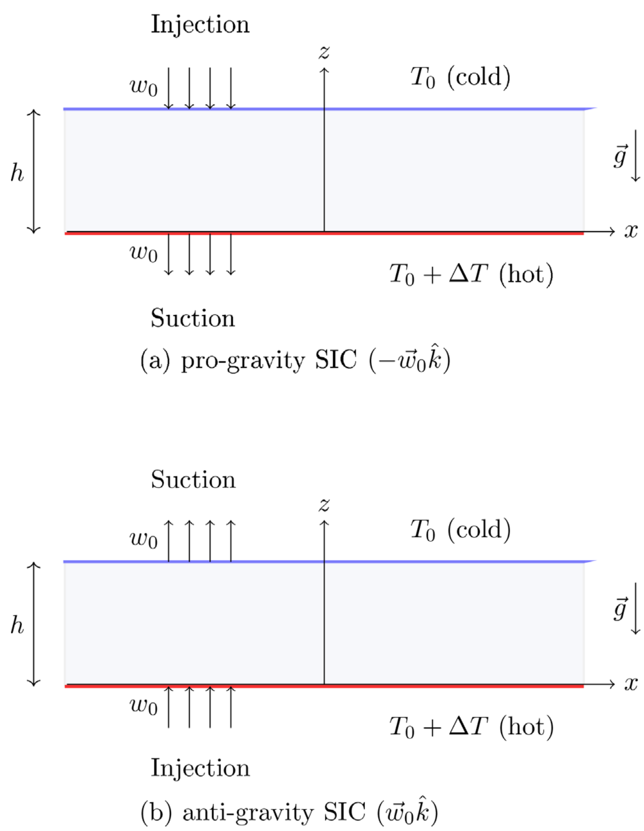

FIG. 1. Schematic of the RBCS with the SIC.

assumed to be free/rigid and perfect conductors of heat as shown in Table I.

The governing equations describing the RBCS in a Boussinesq fluid are the equations of conservation of mass, linear momentum, energy, and equation of state[3] as given below:

$$\nabla \cdot \vec{q} = 0, \tag{1}$$

$$\rho_0 \frac{\partial \vec{q}}{\partial t} = -\nabla p + \mu \nabla^2 \vec{q} + \rho(T)\vec{g}, \tag{2}$$

$$\frac{\partial T}{\partial t} = \chi \nabla^2 T - (\vec{q} \cdot \nabla)T, \tag{3}$$

$$\rho(T) = \rho_0[1 - \beta(T - T_0)], \tag{4}$$

where $\vec{q} = (u, w)$ is the velocity vector in m/s, t is the time in s, p is the pressure in Pa, $\vec{g} = (0, 0, -g)$, acceleration due to gravity in m/s^2, T is the temperature in K, μ, ρ, β, and χ, respectively, represent dynamic viscosity (in kg/ms), density (in kg/m^2), thermal expansion coefficient (in 1/K), and thermal diffusivity (in m^2/s). In writing Eq. (2), we have invoked the "small scale convection motion" approximation.

Due to the assumption of a constant vertical flow, at the quiescent basic state, we have

$$\vec{q}_b = (0, w_0), \quad T_b = T_b(z) \quad \text{and} \quad \rho_b = \rho_b(z), \tag{5}$$

where the subscript b denotes the quantities in the basic state and w_0 represents the strength of the imposed constant suction/injection. Substituting Eq. (5) in Eqs. (1)–(4) and solving the resulting equations, we get the solution at the basic state as

$$\begin{aligned} \vec{q}_b &= (0, w_0), \quad T_b(z) = T_0 + \Delta T f(z), \\ p_b(z) &= -\int \rho_b(z) g dz + c, \\ \rho_b(z) &= \rho_0[1 - \beta \Delta T f(z)], \end{aligned} \tag{6}$$

where $f(z) = \frac{e^{Pe} - e^{\frac{Pez}{h}}}{e^{Pe}-1}$, c is a constant of integration, and $Pe = \frac{w_0 h}{\chi}$, the Peclet number, which characterizes the rate of injection and suction of fluid.

On the quiescent basic state, we superimpose finite amplitude perturbations in the form:

$$\vec{q} = \vec{q}_b + \vec{q}', \quad T = T_b(z) + T', \quad \rho = \rho_b(z) + \rho', \quad p = p_b(z) + p', \tag{7}$$

where the prime indicates a perturbed quantity. Since we consider only two-dimensional disturbances, we introduce the stream function, ψ, as

$$u' = -\frac{\partial \psi'}{\partial z}, \quad w' = \frac{\partial \psi'}{\partial x}. \tag{8}$$

Eliminating the pressure in Eq. (2), incorporating the quiescent state solution and non-dimensionalizing the resulting equation as well as Eq. (3) using the following definition:

$$(x^*, z^*) = \left(\frac{x}{h}, \frac{z}{h}\right), \quad t^* = \frac{\chi}{h^2} t, \quad \psi^* = \frac{\psi'}{\chi}, \quad T^* = \frac{T'}{\Delta T}, \tag{9}$$

we obtain the dimensionless form of the vorticity and heat transport equations as (after removing asterisk)

$$\frac{1}{Pr} \frac{\partial}{\partial t}(\nabla^2 \psi) = Ra \frac{\partial T}{\partial x} + \nabla^4 \psi, \tag{10}$$

$$\frac{\partial T}{\partial t} = \frac{\partial \psi}{\partial x} g(z) + \nabla^2 T - Pe \frac{\partial T}{\partial z} - J(\psi, T), \tag{11}$$

where the non-dimensional parameters are

$$Pr = \frac{\mu}{\rho_0 \chi} \quad \text{and} \quad Ra = \frac{\rho_0 \beta g \Delta T h^3}{\chi \mu},$$

respectively, the Prandtl number that characterizes the working fluid properties, the Rayleigh number that is the eigenvalue of the RBCS problem, and this represents the ratio of forces effecting the flow and forces opposing the flow. The parameter, $g(z) = \frac{Pe}{e^{Pe}-1} e^{Pez}$, involves Pe, J is the Jacobian term, and ∇^2 is the Laplacian operator.

The vorticity and the heat transport equations are solved using the following boundary conditions:

TABLE I. The three different bounding surfaces considered in the study.

Nature of the velocity boundary condition	Nature of the temperature boundary condition	Velocity boundary condition
Both the bounding surface are free (free-free)	Isothermal	$w = \frac{\partial^2 w}{\partial z^2} = 0$ $T = T_0$ at $z = h$ $w = \frac{\partial^2 w}{\partial z^2} = 0$, $T = T_0 + \Delta T$ at $z = 0$
The top bounding surface is free and bottom bounding surface is rigid (free-rigid)	Isothermal	$w = \frac{\partial^2 w}{\partial z^2} = 0$, $T = T_0$ at $z = h$ $w = \frac{\partial w}{\partial z} = 0$, $T = T_0 + \Delta T$ at $z = 0$
Both the bounding surface are rigid (rigid-rigid)	Isothermal	$w = \frac{\partial w}{\partial z} = 0$, $T = T_0$ at $z = h$ $w = \frac{\partial w}{\partial z} = 0$, $T = T_0 + \Delta T$ at $z = 0$

(i) For the case of the upper and lower free, isothermal bounding surface (FIFI), we have

$$\psi = \nabla^2\psi = T = 0 \quad \text{at } z = 0, 1. \tag{12}$$

(ii) For the case of the upper and lower rigid, isothermal bounding surface (RIRI), we have

$$\psi = \nabla\psi = T = 0 \quad \text{at } z = 0, 1. \tag{13}$$

(iii) For the case of the upper bounding surface is free, isothermal and lower bounding surface is rigid, isothermal (FIRI), we have

$$\begin{aligned} \psi = \nabla\psi = T = 0 \quad &\text{at } z = 0 \\ \psi = \nabla^2\psi = T = 0 \quad &\text{at } z = 1. \end{aligned} \tag{14}$$

The normal mode solution of the vorticity and heat transport equations under the assumption of the principle of exchange of stabilities[19] is the following minimal Fourier series representation:

$$\psi(x,z) = \sin(\alpha x)F(z), \tag{15}$$
$$T(x,z) = \cos(\alpha x)G(z), \tag{16}$$

where

$$\begin{bmatrix} E_1(x,z) \\ E_2(x,z) \end{bmatrix} = \begin{bmatrix} \sin(\alpha x)F(z) \\ \cos(\alpha x)G(z) \end{bmatrix}$$

and α is the wave number. The z-dependent functions, $F(z)$ and $G(z)$, are chosen in such a way that they have to satisfy the boundary conditions. The eigenfunctions E_1 and E_2 satisfy the orthogonality conditions:

$$\begin{aligned} \langle E_1^2(x,z)\rangle \neq 0, \quad E_2^2(x,z) >\neq 0, \\ \langle E_1(x,z)E_2(x,z)\rangle = 0, \end{aligned} \tag{17}$$

where $\langle\cdots\rangle = \int_0^{\frac{2\pi}{\alpha}}\int_0^1(\cdots)dz\,dx$ is integration over one wavelength.

Substituting Eqs. (15) and (16) into the steady state, linear version of Eqs. (10) and (11), we get

$$\begin{aligned} F'''' - 2\alpha^2F'' + \alpha^4F - \alpha RaG = 0, \\ G'' - \alpha^2G - PeG' + \alpha gF = 0, \end{aligned} \tag{18}$$

with boundary conditions:

$$\begin{aligned} &F = F'' = G = 0 \quad \text{at } z = 0, 1 \quad \text{for FIFI} \\ &F = F' = G = 0 \quad \text{at } z = 0, 1 \quad \text{for RIRI} \\ &\left.\begin{aligned} F = F' = G = 0 \quad \text{at } z = 0 \\ F = F'' = G = 0 \quad \text{at } z = 1 \end{aligned}\right\} \quad \text{for FIRI.} \end{aligned} \tag{19}$$

We assume the Maclaurian series expansion for the eigenfunctions $F(z)$ and $G(z)$ as

$$\begin{aligned} F(z) &= \sum_{n=0}^{\infty} c_k z^k, \\ G(z) &= \sum_{n=0}^{\infty} d_k z^k. \end{aligned} \tag{20}$$

Substituting Eq. (20) into Eq. (18) gives the following recurrence relation:

$$\begin{aligned} &(k+4)(k+3)(k+2)(k+1)c_{k+4} \\ &-2\alpha^2(k+2)(k+1)c_{k+2} + \alpha^4c_k - \alpha Rad_k = 0, \\ &(k+2)(k+1)d_{k+2} - \alpha^2d_k + \alpha g_1c_k = 0, \end{aligned} \tag{21}$$

where $g_1 = \frac{Pe}{e^{Pe}-1}$.

The first few terms of the recurrence relation are obtained by using the initial conditions mentioned in Eq. (19). Using these terms and Eq. (20), we obtain $F(z)$ and $G(z)$ that satisfy Eq. (17) for different boundary conditions as follows:

(i) For the case of the upper and lower free, isothermal bounding surface (FIFI), we have

$$\begin{aligned} F(z) = {} & z + \frac{a_1}{6}z^3 - \frac{\alpha}{120}(\alpha^3 - 2a_1\alpha - a_2Ra)z^5 + \frac{\alpha}{720}a_2Pe\,Ra\,z^6 \\ & - \frac{\alpha}{5040}(2\alpha^5 + 3a_1\alpha^3 + 3a_2Ra\alpha^2 - g_1Ra\alpha + a_2Pe\,Ra)z^7 \\ & + \cdots + o(z^N), \end{aligned} \tag{22}$$

$$\begin{aligned} G(z) = {} & a_2z + \frac{a_2}{2}Pez^2 + \frac{1}{6}(a_2\alpha^2 - g_1\alpha + a_2Pe^2)z^3 \\ & + \frac{Pe}{24}(2a_2\alpha^2 - 3g_1\alpha + a_2Pe^2)z^4 \\ & + \frac{1}{120}\left(a_2(\alpha^4 + 2Pe^2\alpha^2 + Pe^4)\right) \\ & \left(-g_1\alpha(\alpha^2 + a_1 + 6Pe^2)\right)z^5 + \cdots + o(z^N). \end{aligned} \tag{23}$$

(ii) For the case of both upper and lower rigid, isothermal bounding surface (RIRI) and for the case of the upper free and lower rigid, isothermal bounding surface (FIRI), we have

$$\begin{aligned} F(z) = {} & \frac{a_1}{2}z^2 + \frac{1}{6}z^3 + \frac{a_1}{12}\alpha^2z^4 + \frac{\alpha}{120}(2\alpha + a_2Ra)z^5 \\ & + \frac{\alpha}{720}(3a_1\alpha^3 + a_2PeRa)z^6 + \frac{\alpha}{5040} \\ & (3\alpha^3 + a_2Ra(Pe^2 + 3\alpha))z^7 + \cdots + o(z^N), \end{aligned} \tag{24}$$

$$\begin{aligned} G(z) = {} & a_2z + \frac{a_2}{2}Pez^2 + \frac{a_2}{6}(\alpha^2 + Pe^2)z^3 \\ & + \frac{1}{24}(a_1\alpha g_1 + a_2Pe(Pe^2 + 2\alpha^2))z^4 + \frac{1}{120} \\ & (-\alpha g_1(1 + 4a_1Pe) + a_2(Pe^4 + 3Pe^2\alpha^2 + \alpha^4))z^5 \\ & + \cdots + o(z^N). \end{aligned} \tag{25}$$

Although in the cases of RIRI and FIRI, the eigenfunction expressions in Eqs. (24) and (25), the quantities a_1 and a_2 differ in the two cases.

In Eqs. (22)–(25), N denotes the number of terms considered in the Maclaurin series. The decision on N was taken by using the D'Alembert's ratio test. We started off by taking $n = 10$ as the test specifies that a large number of terms are to be taken. Subsequently we incremented n by unity and each such time we calculated the ratios of the nth term and the $(n+1)$th term. We stopped the incrementation when the successive ratio remained a constant for a chosen accuracy of 10^{-4} for the wave number. This ensured a very good accuracy in the value of theoretical Rayleigh number too, which was ascertained by validating the results as reported in Table II. The above procedure was adopted for all three boundary combinations for chosen value of Pe.

TABLE II. Quantitative comparison of the results from the present study with Chandrasekhar[3] in the absence of SIC. Here, N refers to the number of terms used in the Maclaurin series.

Nature of the boundaries	Chandrasekhar[3]			Present study ($Pe = 0$)			
	Ra_c	α_c	λ	Ra_c	α_c	λ	N
FIFI	0657.511	2.2214	2.8280	0657.511	2.2214	2.8285	15
FIRI	1100.65	2.6820	2.3420	1100.645	2.6824	2.3424	18
RIRI	1707.762	3.1170	2.0160	1707.759	3.1163	2.016	22

Using the eigenfunction expressions (22)–(23) and (24)–(25) along with the upper boundary conditions, we obtain three algebraic equations in terms of a_1, a_2, and Ra. We solve them for a given set of values of Pe and α. In the neighborhood interval of the critical wave number, α_c, we find a list of values for the unknowns (a_1, a_2, and Ra) and among these, the minimum Ra value gives Ra_c, and the value of α that yields this minimum is α_c.

The Maclaurin series approach adopted in this section gives us a polynomial approximation to the eigenfunctions $F(z)$ and $G(z)$. These, in fact, are the trial functions of a Galerkin procedure. We mention here that the truncated Maclaurin series used here is essentially a higher-order Galerkin procedure but that which has a more scientific basis for the choice of trial functions. The chosen Maclaurin series-based trial functions not only satisfy the boundary conditions but also result in a most minimal residue when substituted into the governing equations.

III. DERIVATION OF THE LORENZ MODEL

To derive the Lorenz model, we use the following minimal Fourier–Galerkin representation:

$$\psi(x,z) = \frac{\sqrt{2}\delta^2}{\alpha}\mathcal{X}(t)\sin(\alpha x)F(z), \tag{26}$$

$$T(x,z) = \frac{1}{\pi r}\mathcal{Y}(t)\cos(\alpha x)G(z) + \mathcal{Z}(t)H(z), \tag{27}$$

where $H(z)$ is given by

$$H(z) = \int_0^z\left[\int_0^\xi DF(z)\,G(z)\,dz\right]d\xi + m_1 e^{Pez}z, \tag{28}$$

and m_1 is to be determined using the boundary condition. It is to be noted here that to recover the exact form of the classical Lorenz model,[20] we have used the scaling for the amplitudes in the following way, i.e.,

$$\delta^2 = (\alpha^2 + \pi^2) \quad \text{and} \quad r = \frac{Ra}{Ra_c}.$$

Equation (28) satisfies the following orthogonality conditions:

$$\langle E_1(x,z)H(z)\rangle = 0, \quad \langle E_2(x,z)H(z)\rangle = 0, \quad \langle H^2(z)\rangle \neq 0. \tag{29}$$

Substituting Eqs. (26) and (27) into Eqs. (10) and (11) and making use of Eqs. (17) and (28) and applying orthogonality conditions (17) and (29), we get

$$\left.\begin{aligned}\frac{d\mathcal{X}}{d\tau_1} &= Pr(-p_1\mathcal{X} + p_2\mathcal{Y}),\\ \frac{d\mathcal{Y}}{d\tau_1} &= p_3\, r\, X - p_4 Y - p_5\mathcal{X}\mathcal{Z}\\ \frac{d\mathcal{Z}}{d\tau_1} &= -bp_6\mathcal{Z} + p_7\mathcal{X}\mathcal{Y},\end{aligned}\right\} \tag{30}$$

where $\tau_1 = \delta^2 t$ and $b = \frac{4\pi^2}{\delta^2}$. The coefficients p_i's are given by

$$\left.\begin{aligned}
p_1 &= -\frac{\left\langle \alpha^4F^2 + F\dfrac{d^4F}{dz^4} - 2\alpha^2F\dfrac{d^2G}{dz^2}\right\rangle}{\delta^2\left\langle -\alpha^2F^2 + F\dfrac{d^2F}{dz^2}\right\rangle},\\
p_2 &= \frac{-\delta^2\langle FG\rangle}{\left\langle -\alpha^2F^2 + F\dfrac{d^2F}{dz^2}\right\rangle}, \quad p_3 = \frac{\langle FG\rangle}{\langle G^2\rangle},\\
p_4 &= \frac{-\left\langle -\alpha^2G^2 + G\dfrac{d^2G}{dz^2}\right\rangle}{\delta^2\langle G^2\rangle}, \quad p_5 = \frac{-\left\langle FG\dfrac{dH}{dz}\right\rangle}{\pi\langle G^2\rangle},\\
p_6 &= -\frac{1}{b\delta^2}\frac{\left\langle H\dfrac{d^2G}{dz^2}\right\rangle}{\langle H^2\rangle}, \quad p_7 = \frac{2}{\pi}\frac{\left\langle\left(F\dfrac{dG}{dz} + G\dfrac{dF}{dz}\right)F\right\rangle}{\langle F^2\rangle}.
\end{aligned}\right\} \tag{31}$$

We now transform the dynamical system in Eq. (30) into the form of the classical Lorenz model by using an appropriate scaling for the amplitudes. Let us consider

$$\mathcal{X} = l_1X, \quad \mathcal{Y} = l_2Y, \quad \mathcal{Z} = l_3Z, \tag{32}$$

where l_1, l_2, and l_3 are chosen in such a way that the transformed equation has a form that resembles the classical Lorenz model.[20]

Substituting Eq. (32) into Eq. (30), we get

$$\left.\begin{aligned}\frac{dX}{d\tau} &= Pr^*\left(-X + \frac{l_2}{l_1}\frac{p_2}{p_1}Y\right),\\ \frac{dY}{d\tau} &= r^*\frac{p_1}{p_2}\frac{l_1}{l_2}X - Y - \frac{p_5}{p_4}\frac{l_1l_3}{l_2}X,\\ \frac{dZ}{d\tau} &= -b^*Z + \frac{p_7}{p_4}\frac{l_1l_2}{l_3}XY,\end{aligned}\right\} \tag{33}$$

where $\tau = p_4\tau_1$, $Pr^* = \frac{p_1}{p_4}Pr$, $b^* = \frac{p_6}{p_4}$, and $r^* = \frac{p_2p_3}{p_1p_4}r$. If we choose, $l_1 = \frac{p_4}{\sqrt{p_5p_7}}$, $l_2 = \frac{p_1}{p_2}l_1$, and $l_3 = \frac{p_1p_4}{p_2p_5}$; then, Eq. (33) takes the form of the classical Lorenz model with modified non-dimensional parameters and is given by

$$\left.\begin{aligned}\frac{dX}{d\tau} &= Pr^*(-X + Y),\\ \frac{dY}{d\tau} &= r^*X - Y - XZ,\\ \frac{dZ}{d\tau} &= -b^*Z + XY.\end{aligned}\right\} \tag{34}$$

We can directly derive the Landau equation from the dynamical system (34), and the same is derived in Sec. IV.

IV. DERIVATION OF THE LANDAU EQUATION

From the second and third equations of the Lorenz system (34), we have

$$Y = \frac{1}{Pr^*}\frac{dX}{d\tau} + X, \tag{35}$$

$$Z = \frac{1}{X}\left(r^* X - Y - \frac{dY}{d\tau}\right). \tag{36}$$

Using the second equation of the Lorenz system (34) in Eq. (36), we get

$$Z = \frac{1}{X}\left[(r^* - 1)X - \frac{dX}{d\tau} - \frac{1}{Pr^*}\frac{d^2X}{d\tau^2}\right]. \tag{37}$$

Substituting Eqs. (35) and (37) into the third equation of the Lorenz model Eq. (32), we get a third-order equation in X. Neglecting higher-order terms, we get the following Landau equation:[4]

$$\frac{dX}{d\tau} = \left(\frac{Pr^*}{b^*(1+Pr^*)}\right)\left[b^*(r^*-1)X - X^3\right]. \tag{38}$$

The analytical solution of Eq. (38) is given by

$$X(\tau) = \frac{\sqrt{Q_1}}{\sqrt{Q_2(1-e^{-2Q_1\tau})X_0 + Q_1 e^{-2Q_1\tau}}}\mathcal{X}_0, \tag{39}$$

where $\mathcal{X}_0$ is the initial condition and $Q_1 = \frac{Pr^*(r^*-1)}{(1+Pr^*)}$ and $Q_2 = \frac{Pr^*}{b^*(1+Pr^*)}$.

We next discuss some of the properties of the dynamical system (21) and, therefore, mention the Hopf Rayleigh number and the trapping region for the system (21).

V. STUDY OF THE DYNAMICAL BEHAVIOR OF THE SYSTEM

Since the dynamical system is now transformed into the classical Lorenz model[20] form as in Eq. (34), it inherits the following properties:[21]

(i) The system (34) has natural symmetry

$$(X, Y, Z) \to (-X, -Y, Z).$$

(ii) The flow is volume contracting since

$$\operatorname{div}\mathbf{X} = -(Pr^* + b^* + 1) < 0,$$

where $\mathbf{X} = (X(\tau), Y(\tau), Z(\tau))$.

(iii) If $0 < r^* < 1$, the origin is the only critical point, and it is a global attractor.

(iv) At $r^* = 1$, there is a bifurcation, and there are two more critical points (post-onset):

$$C_1 = (\sqrt{b^*(r^*-1)}, \sqrt{b^*(r^*-1)}, r^*-1)$$

and

$$C_2 = (-\sqrt{b^*(r^*-1)}, -\sqrt{b^*(r^*-1)}, r^*-1).$$

(v) If $1 < r^* < r_H$, where

$$r_H = \frac{Pr^*(Pr^* + b^* + 3)}{Pr^* - b^* - 1} \tag{40}$$

(the Hopf Rayleigh number), the origin is unstable and C_1 and C_2 are both stable.

(vi) At $r > r_H$, C_1 and C_2 lose their stability by absorbing an unstable limit cycle.

To determine the trapping region of the trajectories of the solution of the Lorenz model (34), a smooth real value potential function, $E(\tau)$, where

$$\frac{d\mathbf{X}}{d\tau} = -\frac{dE}{d\mathbf{X}}, \tag{41}$$

is constructed. The negative sign arises from the analogy with the potential energy.

With

$$\frac{dE}{d\tau} = -\left(\left(\frac{dX}{d\tau}\right)^2 + \left(\frac{dY}{d\tau}\right)^2 + \left(\frac{dZ}{d\tau}\right)^2\right) \le 0. \tag{42}$$

This implies that $E(\tau)$ decreases along trajectories and the motion is always toward lower potential. There are many ways to define $E(\tau)$, which satisfies (42), but we define it in the following way:

$$E = -\left(X\frac{dX}{d\tau} + Y\frac{dY}{d\tau} + [Z - (Pr^* + b^*)]\frac{dZ}{d\tau}\right). \tag{43}$$

Substituting Eq. (34) into Eq. (43), we get

$$E = Pr^* X^2 + Y^2 + b^*\left(Z - \frac{Pr^* + r^*}{2}\right)^2 - b^*\left(\frac{Pr^* + r^*}{2}\right)^2. \tag{44}$$

Since E is positive definite, it gives the following ellipsoid as a trapping region:

$$\frac{X^2}{\mathtt{a}^2} + \frac{Y^2}{\mathtt{b}^2} + \frac{(Z - \mathtt{d})^2}{\mathtt{c}^2} = 1, \tag{45}$$

where

$$\mathtt{a} = \sqrt{\frac{b^*}{Pr^*}}\frac{(Pr^* + r^*)}{2}, \quad \mathtt{b} = \sqrt{b^*}\frac{(Pr^* + r^*)}{2},$$
$$\mathtt{c} = \frac{(Pr^* + r^*)}{2}, \quad \text{and} \quad \mathtt{d} = \frac{(Pr^* + r^*)}{2}.$$

In Sec. VI, we discuss the results obtained from the linear and weakly nonlinear stability analyses.

VI. RESULTS AND DISCUSSION

Before we move on to the results and discussion, it is necessary to comment about the choice of Pe considered in the study, viz., the range $[-0.2, 0.2]$. This range was to ensure that features of RBCS remain intact while noticing significant change in regular and chaotic motions even with weak SIC. This approach of considering weak SIC was adopted earlier by Krishnamurti[7] in her experimental work on RBCS.

Using the eigenfunctions in the form defined in Eqs. (22)–(25) obtained by taking $N = 15$ for *FIFI*, $N = 18$ for *FIRI*, and $N = 22$ for *RIRI*, we obtain Ra_c, α_c, and the wavelength, λ. As mentioned earlier, the value of N is decided by using the ratio test on considering the convergence of Ra_c and α_c to its exact value obtained by Chandrasekhar[3] in the limiting case of $Pe = 0$ and the same is listed in Table II. As the table reveals, for the chosen value of N, we found exact values of Ra_c,

α_c, and λ. This validates the numerical results obtained in the paper with a desired accuracy by using the Maclaurin series expansion.

Using a linear stability analysis, we have plotted Ra_c and α_c against Pe in Fig. 2. For plotting α_c against Pe, we used the least squares curve fit with maximum error being of order 10^{-4}. It is clear from these plots that for symmetric boundaries, the influence of Pe in the cases of pro-gravity and anti-gravity remains same and is symmetric as far as Ra_c and α_c are concerned. For asymmetric boundaries, in the case pro-gravity SIC, as Pe increases the system gets into a prolonged stable state and the system destabilizes due to an increase in Pe in the case of anti-gravity SIC. This observation is pointed out by Nield[10] and others. This information is summarized in Table III. Thus, the quantitative comparison of Ra_c and α_c values in the absence of SIC in Table II and the qualitative comparison of the results of the present study with those of previous investigations in the presence of SIC provided in Table III validate the results obtained by the numerical approach used in the paper.

Using the expression of the streamfunction in Eq. (26) and an analytical solution of the Landau equation (39), we have plotted the streamlines in Fig. 3 for different boundary conditions and for different cases of SIC. The shrinking of the cell size due to the boundary conditions is clearly observed in these plots. Furthermore, these plots show that the influence of the SIC in the cases of pro-gravity and anti-gravity is to shrink the cell slightly more in the case of symmetric

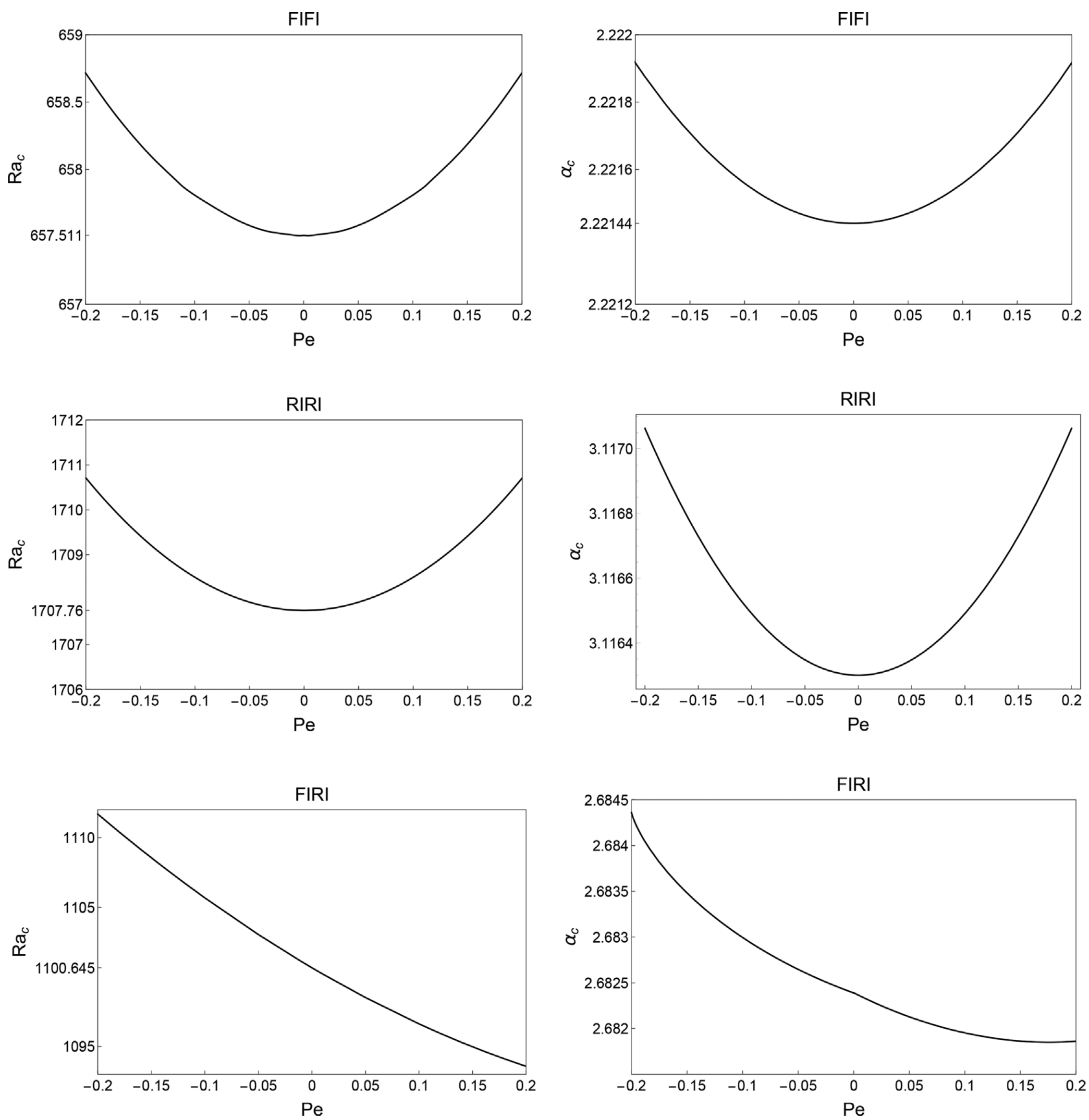

FIG. 2. Plot of Ra_c and α_c vs Pe for symmetric and asymmetric boundaries.

TABLE III. Qualitative comparison of the results from the present study with the previous investigations in the presence of SIC.

Author	Nature of the boundaries	Description of the problem	Method used	Results that match with the present study
Shvartsblat[9]	RIRI	Rayleigh–Bénard convection in the presence of transverse flow (pro-gravity SIC)	Bubnov–Galerkin method	The transverse flow in the layer leads to increase in the values of the critical Rayleigh number
Nield[10]	Symmetric boundaries (both the boundaries are rigid or free)	Rayleigh–Bénard convection in the presence of transverse flow (pro-gravity SIC)	One term Galerkin method with an appropriate polynomial as eigenfunctions	The effect of throughflow is to increase the value of the critical Rayleigh number.
	Asymmetric boundaries (the top boundary is free, and bottom boundary is rigid)			(i) The effect of small amount of throughflow is to decrease the value of the critical Rayleigh number. (ii)The decrement in the value of the critical Rayleigh number is significant if the Peclet number is very much smaller than unity. (iii) The effect of throughflow is large when the Prandtl number is small

boundaries while it is opposite effect in the case of anti-gravity for asymmetric boundaries. These results match with results in Fig. 2 observed in the case of α_c for different boundary conditions.

The occurrence of chaos in the modified Lorenz model is monitored using the values of Hopf Rayleigh number, r_H, and is calculated by using Eq. (40). Using this value of r_H, for different values of Pe, Fig. 4 is plotted for the three boundary conditions considered. It is clear from these plots that the value of r_H for FIFI is less than that of *RIRI*, and this value for FIRI lies between FIFI and RIRI, which is the effect of boundaries we noticed even in the case of Ra_c. However, from these plots, we found an interesting result that the influence of Pe on r_H is exactly opposite to that on Ra_c. This result is mainly due to the influence of Pe on non-dimensional parameters; the Prandtl number (Pr^*), the physical dimension of the layer (b^*), and the scaled Rayleigh number (r^*).

The influence of the SIC on the non-dimensional parameters is summarized in Table IV. It is clear from Table IV that the influence of pro-gravity ($Pe < 0$) and anti-gravity ($Pe > 0$) SIC is to decrease the value of these non-dimensional parameters in the case of symmetric boundaries. However, for asymmetric boundaries, the influence of pro-gravity SIC is to increase Pr^* and decrease b^* and r^* while the influence of anti-gravity SIC is opposite to that of Pr^* and b^*, i.e.,

$$\begin{aligned} Pr^*_{(FIFI)} &< Pr^*_{(FIRI)} < Pr^*_{(RIRI)}, \\ b^*_{(FIFI)} &< b^*_{(FIRI)} < b^*_{(RIRI)}, \\ r^*_{(FIFI)} &> r^*_{(FIRI)} > r^*_{(RIRI)}. \end{aligned} \tag{46}$$

This represents the importance of the choice of boundary conditions in vertical flow problems. The behavior of the Lorenz system (34) greatly depends on the range of these parameters.[21] Thus, we see that though the primary intention of bringing the SIC effect is to control the convection of the system it also helps in controlling the dynamical behavior of the system, and one could use the SIC as a control mechanism to advance or delay the onset of chaos.

Using the indicators, LLE, the time series, the amplitude spectrum, and the phase space plots, we study the dynamical behavior of the system.[22,23] To plot these figures, we have done a numerical integration of the modified Lorenz model (34) using the classical fourth-order Runge–Kutta method with a step size of 0.0005. The LLE quantifies the divergence between two initially close trajectories of the vector field. Therefore, it is used to determine chaotic (LLE >0) and the periodic (LLE $=0$) regimes. The LLE plots in Figs. 5 and 6 indicate the appearance of chaos and the periodic motion in the modified Lorenz model in the presence/absence of the SIC and for symmetric and asymmetric boundaries. The change in the dynamical behavior of the system due to the presence of Pe is demonstrated using the binary indicator as an inset in these plots. This binary indicator is plotted based on the values of LLE being same (in same state) or different, i.e., if LLE value is near to zero (periodic state) for the two cases considered, viz., $Pe = 0$ and $Pe \neq 0$, then the binary code represents the green color otherwise the yellow color. From these plots, we notice that

(a) For both symmetric and asymmetric boundaries, the value of r_H is changes only slightly when we have the SIC effect irrespective of it is being pro-gravity or anti-gravity.

(b) Once chaos sets in, the existence of the periodic motion ($LLE = 0$) or the nearly periodic motion ($LLE \ll 1$) has a lag between two cases of $Pe = 0$ and $Pe \neq 0$. This lag grows exponentially as r^* increases.

(c) For the given range of values of r^*, in all the cases, we can find a largest periodic interval where both $Pe = 0$ and $Pe \neq 0$ have a common behavior of periodic motion for certain values of r^*, except in the case of FIRI boundaries for anti-gravity SIC where for given range of r^* there is no appearance of periodic interval although there are many short burst of dips.

(d) By comparing with free boundaries, for rigid boundaries the number of dips is less. In other words, the chaotic motion is more vigorous for the RIRI boundary compared to the FIFI.

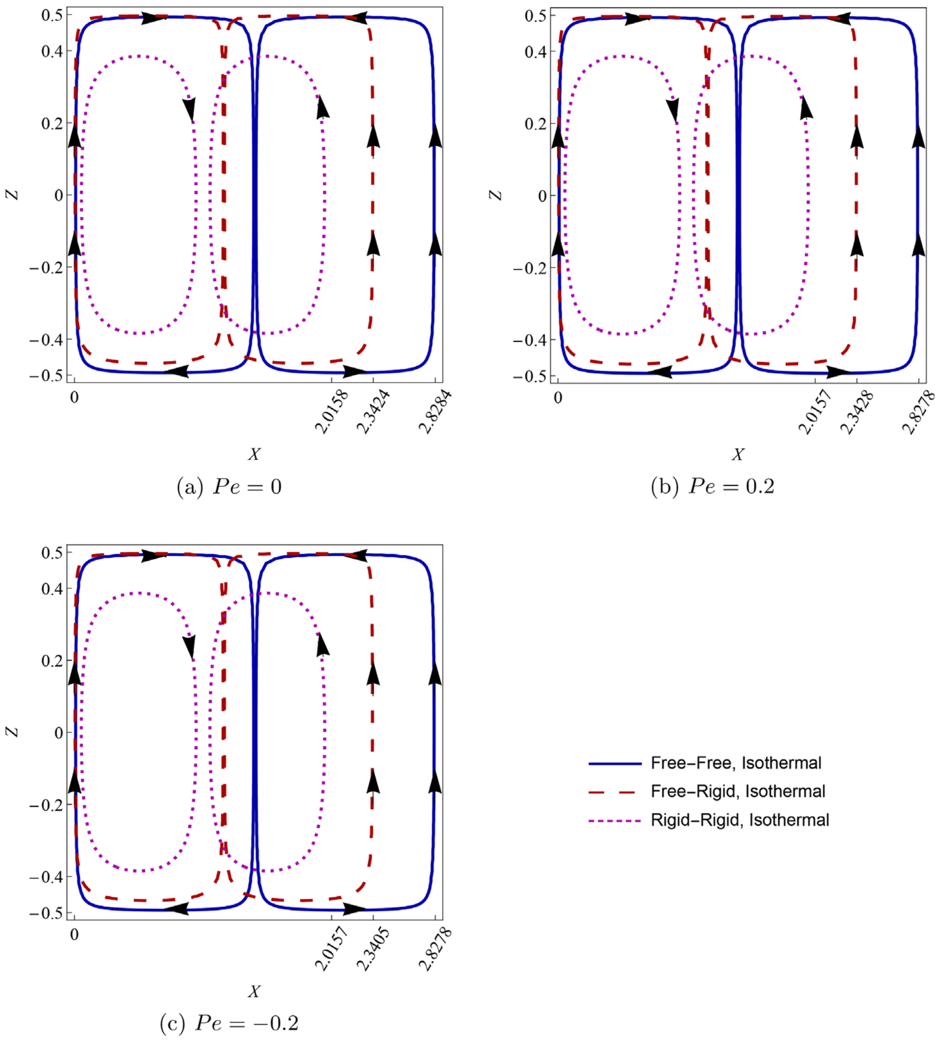

FIG. 3. Streamline plot for $|\psi| = 0.002$ for symmetric and asymmetric boundary conditions and for two values of *Pe*.

The appearance of periodic intervals or dips, thus, depends on the boundary conditions and also on the parameters' values. If we recollect the argument of Sparrow[21] in his book, appearance of anomalous periodic orbits depends on the value of r^* and b^*, more specifically for small values of b^* and large values of r^*. It is evident from Table V that compared to FIFI, in the case of FIRI and RIRI boundaries, the value of b^* is large and r^* is very small, which is exactly the opposite of the case studied by Sparrow.[21] In the current paper, we noticed the opposite result, i.e., less number of periodic points/interval, and in the case of FIRI anti-gravity SIC, there is no periodic interval.

To understand further the behavior of the dynamical system at the largest periodic interval in the range of r^* considered, we have picked a value of r^* at which both the cases $Pe = 0$ and $Pe \neq 0$ have similar behavior of periodic motion. For these values of r^*, we have plotted LLE for different values of *Pe* in the range of $[-0.2, 0.2]$. Figure 7 presents these plots. It is clear from LLE plots that at certain fixed r^* value, for symmetric boundaries, this common behavior of the periodic motion is observed for all values of *Pe* in $[-0.2, 0.2]$. However, for asymmetric boundaries at $Pe = -0.2$ and $Pe \ll 0$, we notice such a common behavior of periodic motion and for other values of *Pe* there is a chaotic motion. This common periodic behavior for symmetric boundaries and the strange chaotic behavior for asymmetric boundaries is further studied in detail by using the time series, the amplitude spectrum, and phase space plots in Figs. 8 and 9.

The time series and the phase space plots in Figs. 8 and 9 provide information about the number of limit cycles for the considered cases. For FIFI boundaries, it is a 2-cycle and, for RIRI boundaries, it is a 3-cycle, and this is irrespective of the values of *Pe* in the range $[-0.2, 0.2]$. The amplitude spectrum of a time series is widely used as a first test for studying the dynamical behavior of the system where we use Fourier methods in which a finite-length digital signal in time domain is represented in the frequency domain. This gives the distribution of the amplitude as a function of the components of frequencies. In Figs. 8 and 9, the amplitude spectrum is plotted using 200 000 data points with a time step of 0.05. For $Pe = 0$, it is pretty clear from the amplitude spectrum plots in Fig. 8 in the case of symmetric boundaries that there

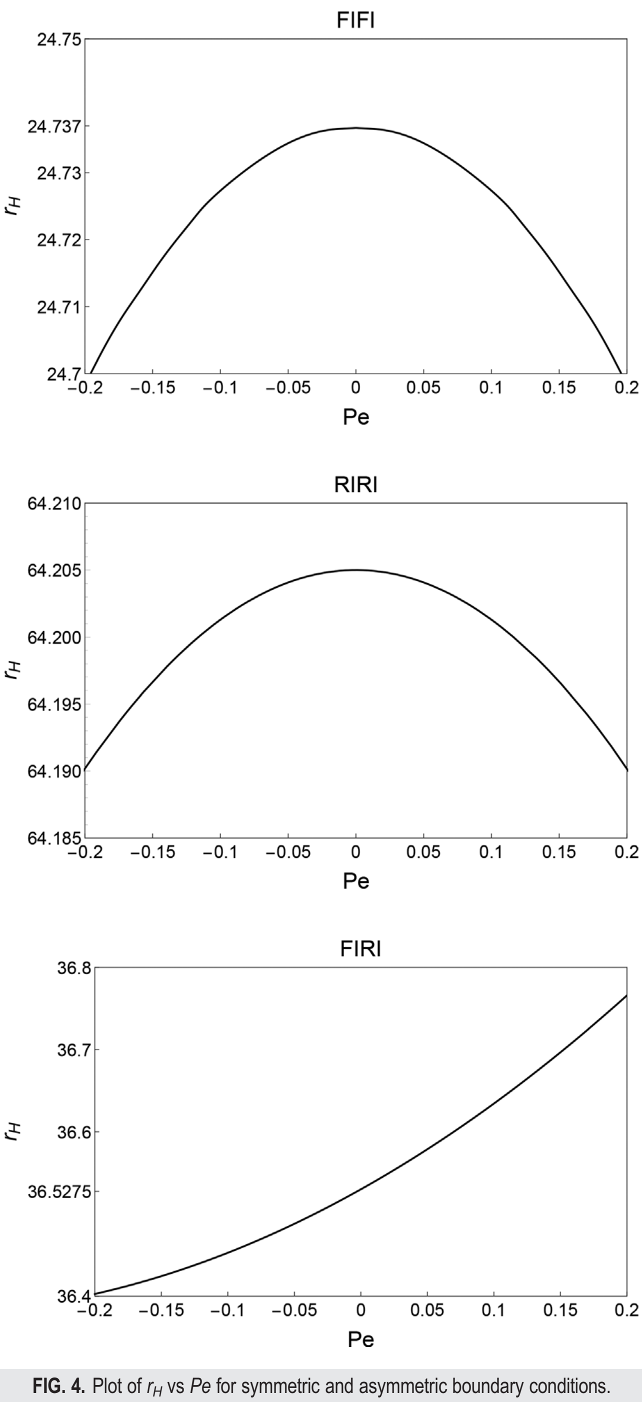

FIG. 4. Plot of r_H vs Pe for symmetric and asymmetric boundary conditions.

TABLE IV. Values of the scaled non-dimensional parameters of the Lorenz model (34) for different values of Pe and for the cases of three different boundaries.

Nature of boundaries	Pe	$\frac{Pr^*}{Pr}$	$\frac{b^*}{b}$	$\frac{r^*}{r}$
FIFI	± 0.2	0.99880	0.99450	0.99815
	0	1	1	1
FIRI	-0.2	1.44986	1.444820	0.62598
	0	1.44028	1.511790	0.62720
	0.2	1.42819	1.58204	0.62631
RIRI	± 0.2	1.95250	2.01545	0.45213
	0	1.95412	2.02597	0.45278

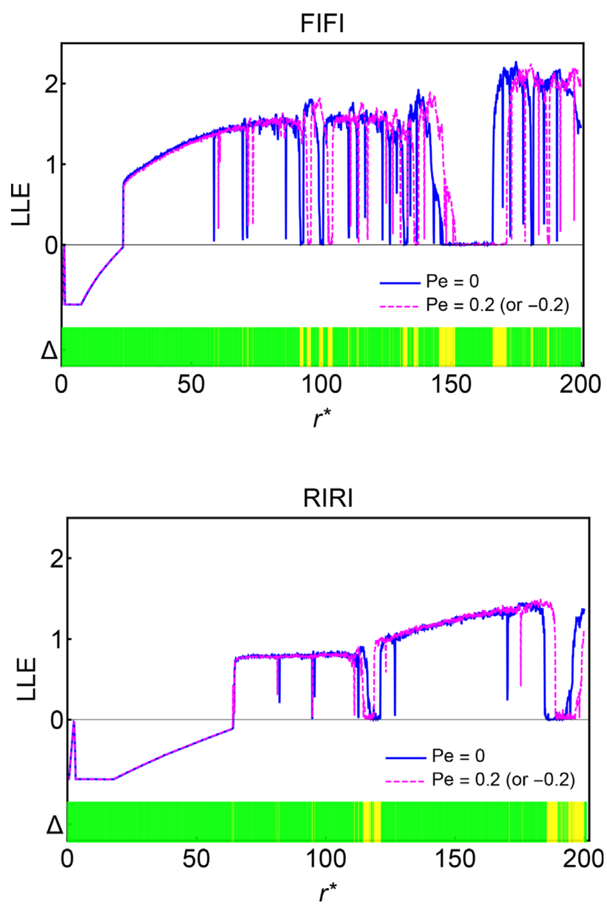

FIG. 5. Plot of LLE vs r^* for different values of Pe and for symmetric boundaries.

is a finite number of frequency components in a given frequency range, and hence, the majority of the amplitudes and, therefore, the power is distributed within first three frequencies. Furthermore, the amplitude of these frequency components' distribution slightly varies when we consider $Pe \neq 0$. The finite number of frequencies is the signature of a periodic sequence or a regular time series.

Now coming to the discussion on FIRI boundaries for different values of Pe using Fig. 9, it is clear that unlike in the case of symmetric boundaries where the amplitude spectrum shows a finite number of frequency components and majority of the amplitudes are distributed between first three frequencies, in FIRI boundaries, we notice that the distribution of amplitudes is made among many frequencies

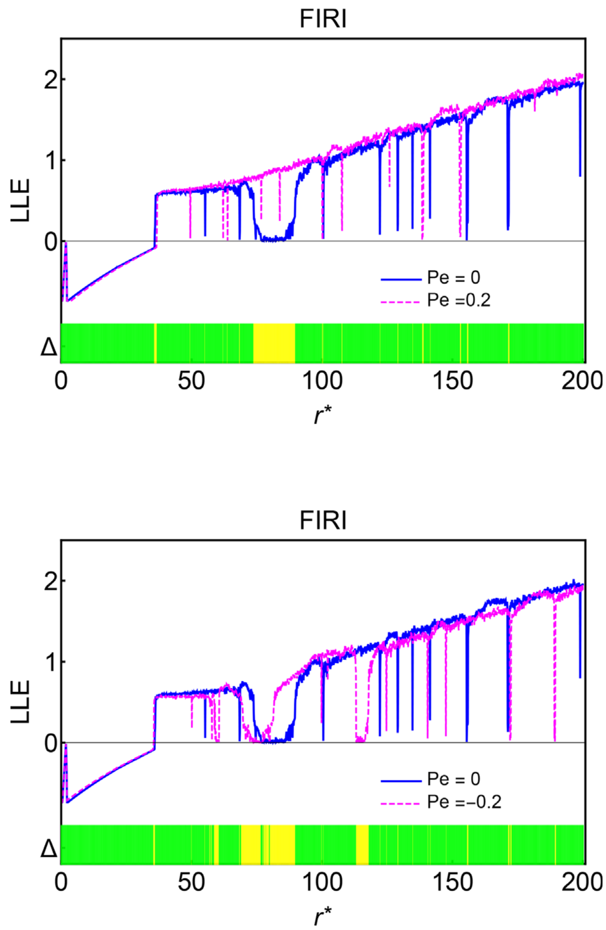

FIG. 6. Plot of *LLE* vs r^* for different values of *Pe* and for asymmetric boundaries.

(although not infinitely many) with some white noise in the case of pro-gravity SIC and without any noise in the case of no SIC. However, in the case of anti-gravity, as may be expected, it consists of an infinite number of frequencies, indicating an irregular time series and, therefore, a chaotic motion. Thus, although there are particular values of r^* where the appearance of periodic behavior is common (except in the case of FIRI boundaries for anti-gravity case), the periodicity changes. The information on the onset of chaos, the first largest periodic intervals (FLPI), and the periodicity at these intervals for all the cases considered are summarized in Table V. It is quite clear from this table that the values of r^* for plotting Figs. 7–9 are chosen from FLPI.

TABLE V. Information on the values of r_H and the first largest periodic interval (FLPI) and periodicity in that interval for different cases of SIC and for symmetric and asymmetric boundaries.

Nature of the boundaries	*Pe*	r_H	FLPI	Periodicity in FLPI
FIFI	0	24.74	[146.9, 166.1]	2
	±0.2	24.70	[151.8, 171.5]	2
RIRI	0	64.21	[185.1, 193.4]	3
	±0.2	64.19	[189, 196.7]	3
FIRI	−0.2	36.40	[72.1, 86.3]	2
	0	36.53	[72.5, 80.1]	3
	0.2	36.77	…	…

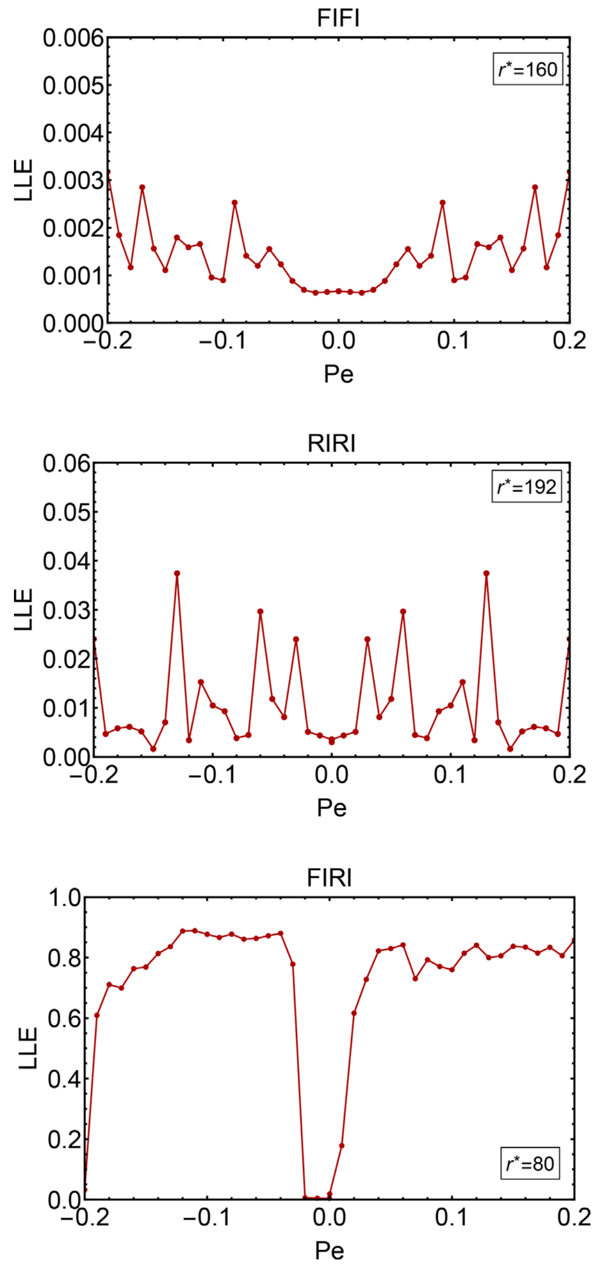

FIG. 7. Plot of *LLE* vs *Pe* for a particular value of r^* chosen from the largest periodic interval and for symmetric and asymmetric boundaries.

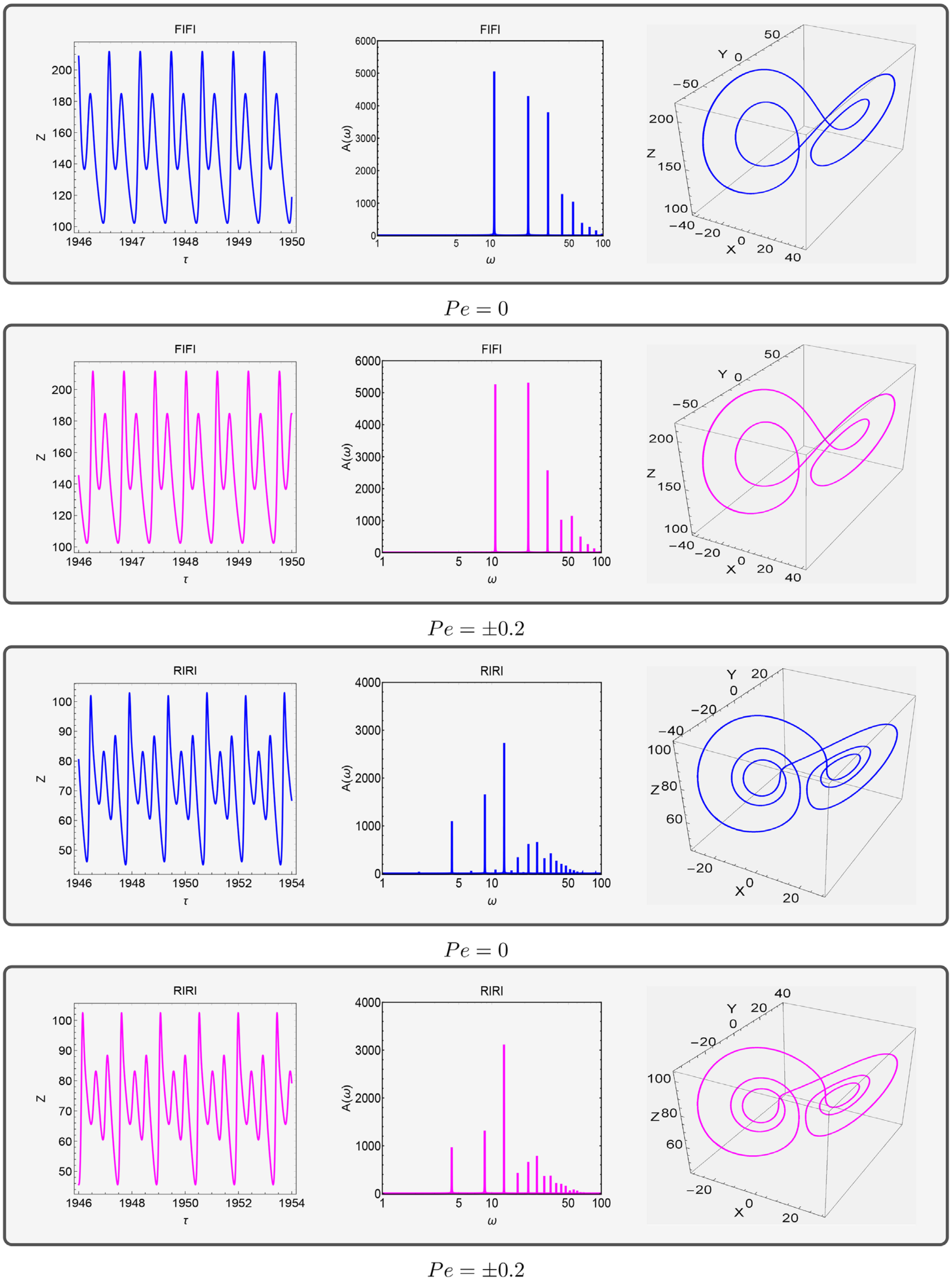

FIG. 8. Plots of the time series, the amplitude spectrum, and phase space plot for different values of *Pe* and for symmetric boundary conditions by taking the value of r^* from the largest periodicity interval.

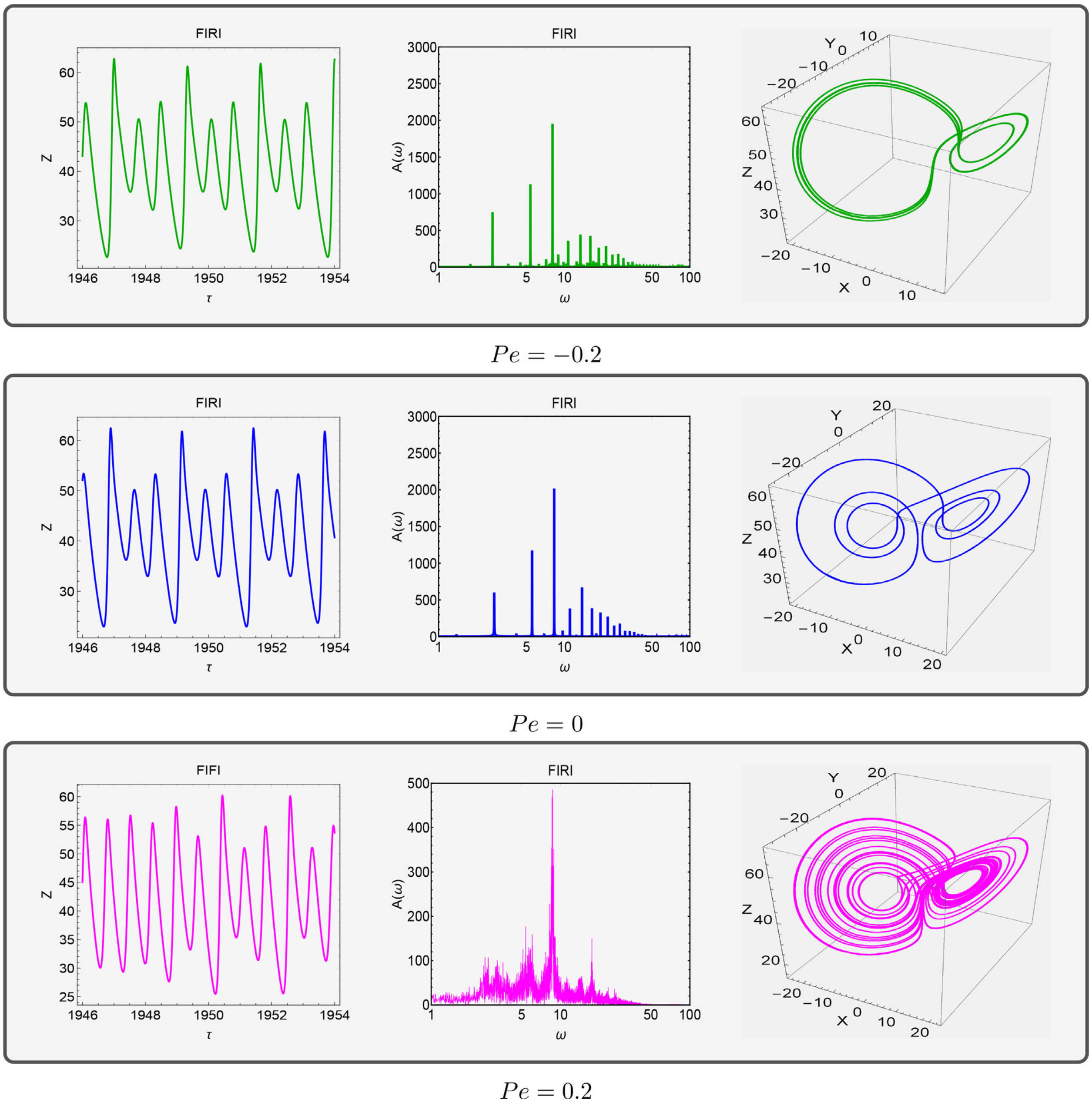

FIG. 9. Plots of the time series, the amplitude spectrum, and phase space plot for different values of *Pe* and for asymmetric boundary conditions by taking the value of r^* to be 80.

To explore more on boundary conditions' influence on the dynamics of the system the difference plots (a) between FIFI, and RIRI in the case of pro-gravity and anti-gravity SIC (b) between FIFI, and FIRI in the case of pro-gravity and, (c) between FIFI and FIRI in the case of anti-gravity are presented in Fig. 10. From these plots, it is clear that the difference is remarkable in the case of (a) where the difference is of 42.23% while in the case of (b) it is 21% and in the case of (c), it is 30.38%. Further in the case of (a), the difference is high in the neighborhood of r_H and it is carried forward to each periodic dip. The vigorous chaotic motion in the case when the boundary is rigid is the main reason for this difference in the values.

As we noticed in the case of convective cell size, in the streamline plots in Fig. 3, there is an exactly similar observation to be made on the trapping region too (where the system is bounded and trajectories remains inside an ellipsoid with principle axis in the *y*-direction) as shown in Fig. 11. The volume of the ellipsoid is drastically reduced in the case of rigid boundaries when compared to that of other boundaries. Furthermore, the size of the trapping region shrinks when the

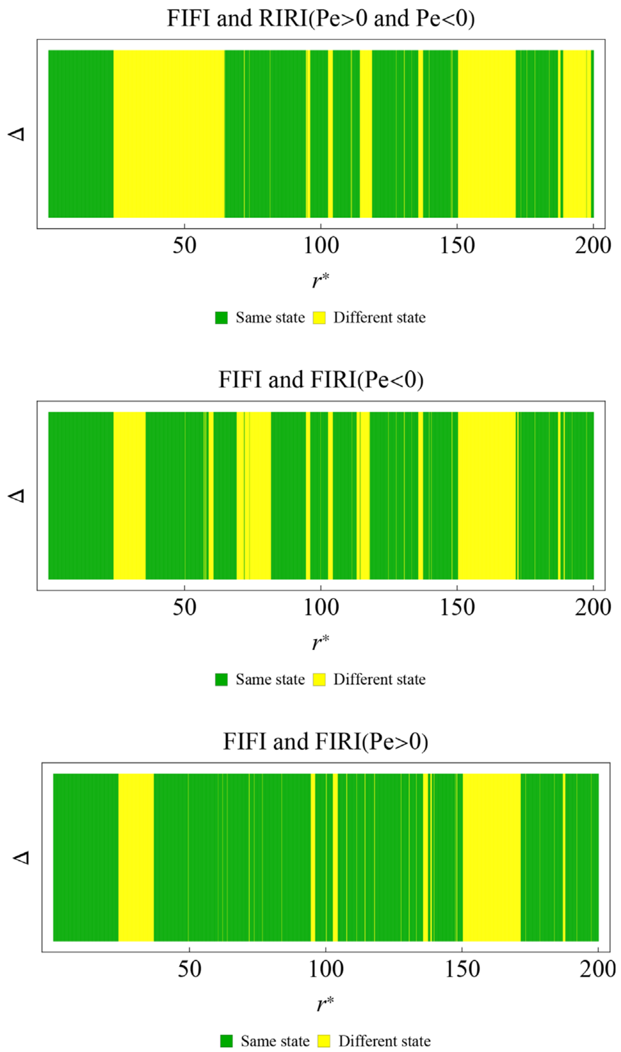

FIG. 10. Plot of *LLE* vs r^* for different values of *Pe* and for asymmetric boundaries.

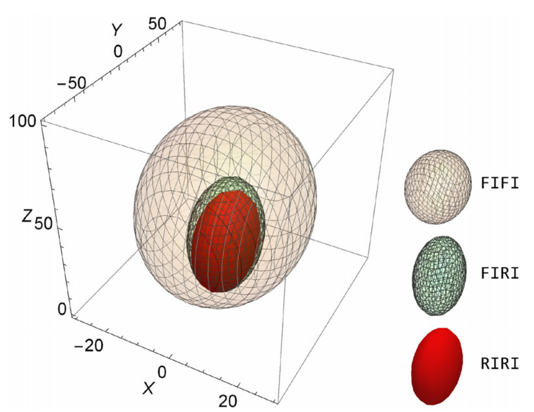

FIG. 11. The trapping region for all the boundary conditions, for $Pe = 0$.

TABLE VI. Lengths of the major axis, minor axis, center, and the volume of the ellipsoid, which is the trapping region for the modified Lorenz model, for different cases of the SIC and for three different boundaries.

Nature of the boundaries	*Pe*	a (m)	b (m)	c (m)	Center	Volume $\times 10^{-4}$ (m^3)
FIFI	0	23.24	73.48	45.00	(0,0,45)	32.18
	±0.2	23.13	73.09	44.92	(0,0,44.92)	31.80
RIRI	0	8.17	36.11	25.37	(0,0,25.37)	3.14
	±0.2	8.15	36.00	25.36	(0,0,25.36)	3.12
FIRI	−0.2	9.23	35.16	29.25	(0,0,29.25)	3.98
	0	9.46	35.91	29.20	(0,0,29.20)	4.16
	0.2	9.70	36.65	29.41	(0,0,29.41)	4.34

SIC effect is considered in the case of symmetric boundaries whereas in the case of asymmetric boundaries it shrinks for the pro-gravity SIC case and enlarges for the anti-gravity SIC case (Table VI).

VII. CONCLUSION

The study on the effect of the SIC on linear and weakly nonlinear stability of the RBCS in the cases of symmetric and asymmetric boundary conditions using a Maclaurin series results in the following general conclusions:

(i) For symmetric boundaries, the critical Rayleigh number, wave number, and the streamline plots for different values of *Pe* reveal that the influence of the SIC is to stabilize the system irrespective of SIC being pro-gravity or anti-gravity. For asymmetric boundaries, the corresponding plots for different values of *Pe* reveal that the influence of pro-gravity SIC is to stabilize the system and that of the anti-gravity SIC is to destabilize the system.

(ii) For all cases except the anti-gravity case of FIRI boundaries, the effect of the SIC is to hasten the onset of chaos.

(iii) There is a slight lag in the *LLE* when we compare the cases of $Pe = 0$ and $Pe \neq 0$ and this lag grows exponentially as we increase r^*.

(iv) For FIRI boundaries, when the SIC is anti-gravity, the LLE does not show any dip.

(v) For all cases except the anti-gravity case of FIRI boundary combination, the effect of the SIC is to shrink the trapping region. In the anti-gravity case of FIRI boundaries, it has an opposite effect.

(vi) By comparing with free boundaries, in the case of rigid boundaries, the number of dips decreases. This indicates a vigorous chaotic motion in the case of rigid boundaries.

Like the rectangular RBCS, there does exist the cylindrical RBCS.[24,25] It would be interesting and challenging to consider such problems with throughflow. This work is under progress.

ACKNOWLEDGMENTS

K.C. is grateful to the Universidad de Tarapacá, Chile, for supporting her research work. L.M.P. acknowledges financial support from ANID through Convocatoria Nacional Subvención a

Instalación en la Academia Convocatoria Año 2021, Grant No. SA77210040. D.L. acknowledges partial financial support from Centers of Excellence with BASAL/ANID financing, Grant No. AFB220001, CEDENNA. The authors are grateful to the reviewers for their most useful comments which refined our paper.

AUTHOR DECLARATIONS

Conflict of Interest

The authors have no conflicts to disclose.

Author Contributions

Kanchana C: Conceptualization (equal); Data curation (equal); Formal analysis (equal); Investigation (equal); Methodology (equal); Validation (equal); Visualization (equal); Writing – original draft (equal); Writing – review & editing (equal). **Pradeep G. Siddheshwar:** Conceptualization (equal); Formal analysis (equal); Methodology (equal); Supervision (equal); Validation (equal); Visualization (equal); Writing – review & editing (equal). **Laura M. Pérez:** Conceptualization (equal); Formal analysis (equal); Methodology (equal); Validation (equal); Visualization (equal); Writing – review & editing (equal). **David Laroze:** Conceptualization (equal); Formal analysis (equal); Funding acquisition (equal); Investigation (equal); Methodology (equal); Project administration (equal); Resources (equal); Software (equal); Supervision (equal); Validation (equal); Visualization (equal); Writing – review & editing (equal).

DATA AVAILABILITY

Data sharing is not applicable to this article as no new data were created or analyzed in this study.

REFERENCES

[1]H. Beńard, "Les tourbillons cellularies dans une nappe liquide (the cellular vortices in a liquid layer)," Rev. Gén. Sci. Pures Appl. **11**, 1261–1271 (1900).
[2]Lord Rayleigh, "On convection currents in a horizontal layer of fluid when the higher temperature is on the under side," London, Edinburgh, Dublin Philoso. Mag. J. Sci. **32**, 529–546 (1916).
[3]S. Chandrasekhar, *Hydrodynamic and Hydromagnetic Stability* (Clarendon Press, Oxford, 1961).
[4]J. K. Platten and J. C. Legros, *Convection in Liquids* (Springer, Science & Business Media, New York, 2012).
[5]H. Riehl, *Tropical Meteorology* (McGraw-Hill, 1954).
[6]E. Augstein, H. Schmidt, and F. Ostapoff, "The vertical structure of the atmosphere planetary boundary layer in undisturbed trade winds over the Atlantic ocean," Boundary Layer Meteors **6**, 129–150 (1974).
[7]R. Krishnamurti, "On cellular cloud patterns. Part 1: Mathematical model," J. Atmos. Sci. **32**, 1353–1363 (1975).
[8]G. Z. Gershuni, E. M. Zhukhovitskii, and D. L. Shvartsblat, "On the stability of transverse flow of fluid between permeable boundaries," J. Appl. Math. Mech. **31**, 120–124 (1967).
[9]D. L. Shvartsblat, "The spectrum of perturbations and convective instability of a plane, horizontal fluid layer with permeable boundaries," J. Appl. Math. Mech. **32**, 266–281 (1968).
[10]D. A. Nield, "Throughflow effects in the Rayleigh–Bénard convective instability problem," J. Fluid Mech. **185**, 353–360 (1987).
[11]P. G. Siddheshwar and S. Pranesh, "Suction-injection effects on the onset of Rayleigh–Bénard–Marangoni convection in a fluid with suspended particles," Acta Mech. **152**, 241–252 (2001).
[12]A. Bayliss, T. K. Ma, B. J. Matkowsky, and C. W. Wahle, "The reactive Rayleigh–Bénard problem with throughflow," SIAM J. Appl. Math. **61**, 1103–1142 (2001).
[13]R. A. Wooding, "Rayleigh instability of a thermal boundary layer in flow through a porous medium," J. Fluid Mech. **9**, 183–192 (1960).
[14]F. M. Sutton, "Onset of convection in a porous channel with net through," Phys. Fluids **13**, 1931–1934 (1970).
[15]G. M. Homsy and A. E. Sherwood, "Convective instabilities in porous media with throughflow," AIChE J. **22**, 168–174 (1976).
[16]M. C. Jones and J. M. Persichetti, "Convective instability in packed beds with throughflow," AIChE J. **32**, 1555–1557 (1986).
[17]I. S. Shivakumara, "Boundary and inertia effects on convection in porous media with throughflow," Acta Mech. **137**, 151–165 (1999).
[18]A. Barletta and D. A. Nield, "Linear instability of the horizontal throughflow in a plane porous layer saturated by a power-law fluid," Phys. Fluids **23**, 013102 (2011).
[19]F. Capone, J. A. Gianfrani, G. Massa, and D. A. S. Rees, "A weakly nonlinear stability analysis of the effect of vertical throughflow on Darcy–Bénard convection," Phys. Fluids **35**, 014107 (2023).
[20]E. N. Lorenz, "Deterministic nonperiodic flow," J. Atmos. Sci. **20**, 130–141 (1963).
[21]C. Sparrow, *The Lorenz Equations: Bifurcations, Chaos, and Strange Attractors* (Springer Verlag, New York, 1982).
[22]C. Kanchana, Y. Zhao, and P. G. Siddheshwar, "A comparative study of individual influences of suspended multiwalled carbon nanotubes and alumina nanoparticles on Rayleigh–Benard convection in water," Phys. Fluids **30**, 084101 (2018).
[23]P. G. Siddheshwar, C. Kanchana, and D. Laroze, "A study of Darcy–Bénard regular and chaotic convection using a new local thermal non-equilibrium formulation," Phys. Fluids **33**, 044107 (2021).
[24]P. G. Siddheshwar and K. M. Lakshmi, "Darcy–Bénard convection of Newtonian liquids and Newtonian nanoliquids in cylindrical enclosures and cylindrical annuli," Phys. Fluids **31**, 084102 (2019).
[25]P. G. Siddheshwar, D. Laroze, and K. M. Lakshmi, "A study of the natural convection of water-AA7075 nanoliquids in low-porosity cylindrical annuli using a local thermal non-equilibrium model," Phys. Fluids **33**, 032018 (2021).